FULL TITLE
ASP Conference Series, Vol. **VOLUME**, **YEAR OF PUBLICATION**
NAMES OF EDITORS

3-D Dynamics of Interactions between Stellar Winds and the Interstellar Medium as Seen by AKARI and Spitzer

Toshiya Ueta[1], Hideyuki Izumiura[2], Issei Yamamura[3], Robert E. Stencel[1], Yoshikazu Nakada[4,5], Mikako Matsuura[6], Yoshifusa Ita[3,6], Toshihiko Tanabé[4], Hinako Fukushi[4], Noriyuki Matsunaga[6], Hiroyuki Mito[5], and Angela K. Speck[7]

[1] *Dept. of Physics & Astronomy, University of Denver, USA*
[2] *Okayama Astrophysical Observatory, NAOJ*
[3] *Institute of Space and Astronautical Science, JAXA*
[4] *Institute of Astronomy, Schooof Science, University of Tokyo*
[5] *Kiso Observatory, Institute of Astronomy, University of Tokyo*
[6] *National Astronomical Observatory of Japan*
[7] *Dept. of Physics & Astronomy, University of Missouri, USA*

Abstract. Recent far-infrared mapping of mass-losing stars by the *AKARI Infrared Astronomy Satellite* and *Spitzer Space Telescope* have suggested that far-infrared bow shock structures are probably ubiquitous around these mass-losing stars, especially when these stars have high proper motion. Higher spatial resolution data of such far-infrared bow shocks now allow detailed fitting to yield the orientation of the bow shock cone with respect to the heliocentric space motion vector of the central star, using the analytical solution for these bow shocks under the assumption of momentum conservation across a physically thin interface between the stellar winds and interstellar medium (ISM). This fitting analysis of the observed bow shock structure would enable determination of the ambient ISM flow vector, founding a new technique to probe the 3-D ISM dynamics that are local to these interacting systems. In this review, we will demonstrate this new technique for three particular cases, Betelgeuse, R Hydrae, and R Cassiopeiae.

1. Interactions between Stellar Winds and the ISM

Most stars lose their surface matter into the surrounding interstellar space in one way or another via mass loss (e.g. Willson 2000; Kudritzki & Puls 2000). Such mass loss processes intimately relate these mass-losing stars to the interstellar medium (ISM), which these stars enrich with ashes of nuclear burning taking place inside these stars. Indeed, mass loss is the critical process that one must consider when it comes to the mass budget of the ISM (e.g. Sedlmayr 1994; Matsuura et al. 2009).

When we think of such ISM enrichment by stellar mass loss ejecta, however, we often naïvely expect that stellar ejecta will eventually meet with the ISM and get merged into it without giving serious thought about the process of the stellar ejecta merging with the ISM. On the first order approximation, the wind-ISM merger occurs where the ram pressure of the stellar wind is balanced by the pressure of the ambient ISM: a shock is expected to form if the wind velocity

is greater than the ambient sound speed ($v_{\rm w} > v_{\rm c}$) and a pile-up of the ejecta is anticipated otherwise ($v_{\rm w} < v_{\rm c}$). Either way, a density enhancement ensues at the interface between the stellar wind and ISM. Such density enhancements can be detected if sufficient amount of radiation is induced within the wind-ISM interface regions. Since the wind-ISM interface often occurs surrounding the mass-losing star, we typically detect such density enhancements in the form of concentric arcs around the central star.

Such arc-shaped circumstellar structures had already been found around luminous OB stars and Wolf-Rayet and red supergiant stars (Stencel, Pesce, & Hagen Bauer 1988; Van Buren & McCray 1988) in the far-infrared (far-IR) All-Sky maps obtained by the *Infrared Astronomy Satellite* (*IRAS*). Far-IR emission from these arcs is probably mainly due to thermal emission of the cold dust component of the density enhancement at the wind-ISM interface whose shock-heated temperature peaks at far-IR. There may be contributions from low-excitation atomic lines such as [O I] 63μm, [O I] 145μm and [C II] 158μm at these wavelengths. However, the exact emission mechanism of these far-IR bow shocks remains unclear. While an attempt to identify their spectroscopic nature is currently on-going with the *Spitzer Space Telescope* (*Spitzer*; Werner et al. 2004), this is beyond the scope of the present paper. Below, we will restrict our discussion to concentrate on the structure of these stellar wind-ISM bow shocks and what we can learn from it.

2. 3-D Motions of the Star, Shock, and the ISM

IRAS discoveries of these bow shock structures at the wind-ISM interface were certainly astounding. Nevertheless, the spatial resolution of the *IRAS* observations (typically $2'$ to $5'$) was not sufficient enough to allow detailed structural analyses of the far-IR shock surfaces. To pursue this avenue of research, we had to wait until the far-IR renaissance of this decade with the coming of *Spitzer* and the *AKARI Infrared Astronomy Satellite* (*AKARI*: Murakami et al. 2007), which permit sub-arcminute spatial resolution in the far-IR.

This far-IR renaissance in context of the present study began with a *Spitzer* discovery of a stellar wind bow shock arc around R Hydrae (R Hya), a Mira-type evolved star (Ueta et al. 2006, Figure 1), followed by a revisit to Betelgeuse, one of the first *IRAS* discoveries of a far-IR stellar wind bow shock, using the Far-IR Surveyor instrument (FIS; Kawada et al. 2007) aboard *AKARI* (Ueta et al. 2008, Figure 2). New far-IR images of these sources clearly reveal the characteristic arc-shaped structure of a bow shock at the interface between stellar winds and the ISM at sub-arcminute spatial resolution. For these bow shocks to occur, the mass-losing central star has to be moving *relative to* the ISM that is local to these objects. Indeed, these stars exhibit proper motion that is consistent with the orientation of the bow shocks (i.e. toward the apex of the bow).

Meanwhile, theoretical studies have been done both analytically (Wilkin 1996, 2000) and numerically (e.g. Mac Low et al. 1991; Dgani, Van Buren, & Noriega-Crespo 1996; Blondin & Koerwer 1998; Wareing, Zijlstra, & O'Brien 2007) to understand the structure of these bow shocks. Remarkably, if one assumes momentum conservation across a physically thin (i.e. radiative-cooling dominating) shock layer, one can express the shape of the bow shock analytically as a function of

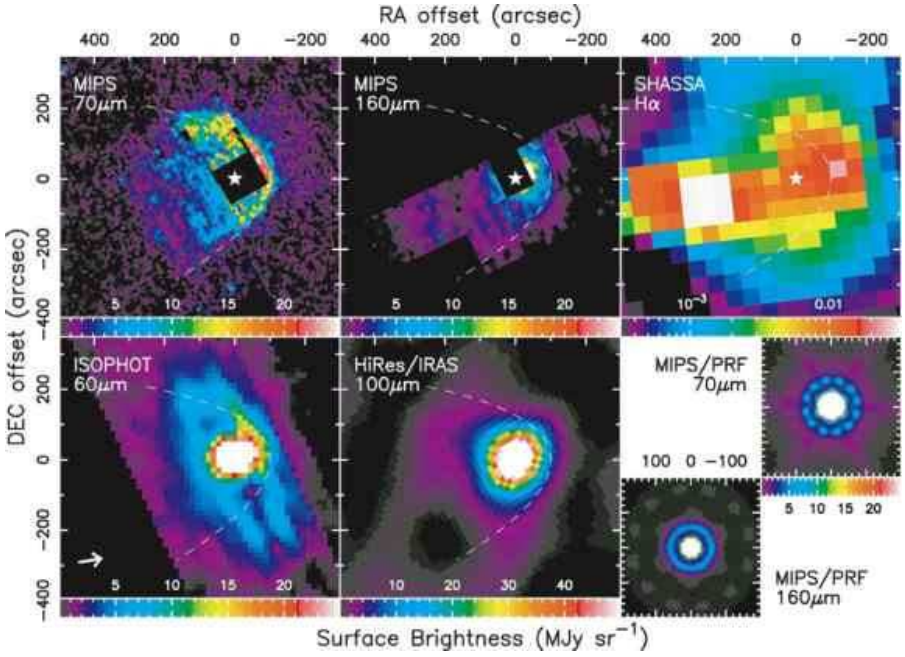

Figure 1. *Spitzer* maps of R Hya at 70 and 160μm (top left and middle, respectively; also shown are the point-response function at these wavelengths at the bottom right) along with an *Infrared Space observatory* map at 60μm (bottom left; Hashimoto & Izumiura 1997) and an *IRAS* map at 100μm (bottom middle; HiRes-processed) as well as a SHASSA Hα map (top right; Gaustad et al. 2001). Tick marks indicate angular offsets in arcseconds with respect to the position of the star. Surface brightness in MJy sr^{-1} is indicated by the scale at the bottom of each panel. A parabolic curve, which roughly represents the shape of the bow shock, is displayed by the dashed lines. The arrow at the bottom left corner shows the direction of the proper motion of the star, $(\mu_\alpha, \mu_\delta) = (-57.68, 12.86)$ mas yr^{-1} (van Leeuwen 2007). Reproduced from Ueta et al. (2006).

the latitudinal angle θ measured from the direction of the bow apex with respect to the position of the central star as follows (Wilkin 1996):

$$R(\theta) = R_0 \frac{\sqrt{3(1 - \theta \cot \theta)}}{\sin \theta} \tag{1}$$

where R_0 is the *stand-off distance* between the star and bow apex defined as

$$R_0 = \sqrt{\frac{\dot{M} v_{\rm w}}{4\pi \rho_{\rm ISM} v_*^2}} \tag{2}$$

for which $\dot{M}$ is the rate of mass loss, $v_{\rm w}$ is an isotropic stellar wind velocity, $\rho_{\rm ISM}$ is the density of the ambient ISM, and v_* is the space velocity of the star.

The observed shape of the bow shock is really a projection of the bow shock cone (eqn.1) onto the plane of the sky (Wilkin 1996). For instance, while the

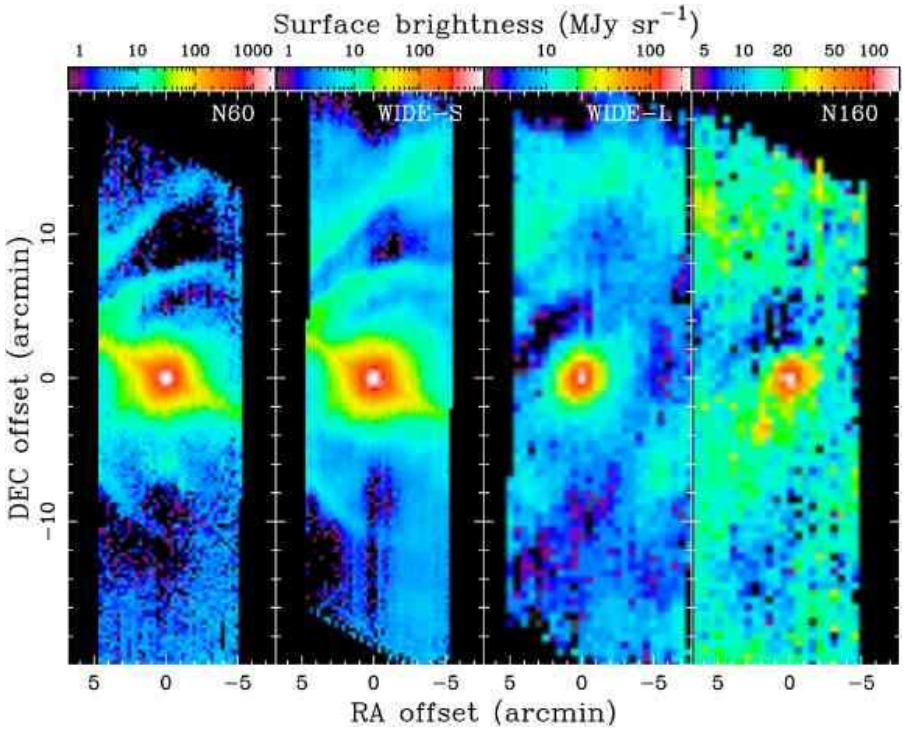

Figure 2. AKARI/FIS maps of Betelgeuse in the SW bands - N60 (65μm) and WIDE-S (90μm) at 15″ pixel^{-1} scale - and in the LW bands - WIDE-L (140μm) and N160 (160μm) at 30″ pixel^{-1} scale - from left to right, respectively. Tick marks indicate angular offsets in arcminutes with respect to the position of the star. Surface brightness in MJy sr^{-1} is indicated by the scale at the top of each panel. The revised *Hipparcos* proper motion is $(\mu_\alpha, \mu_\delta) = (27.54, 11.30)$ mas yr^{-1} (van Leeuwen 2007). Reproduced from Ueta et al. (2008).

R Hya bow appears very close to an edge-on bow shock cone (Figure 1) the Betelgeuse bow looks rather circular (Figure 2), suggesting an inclination angle far from edge-on. At far-IR, the surface brightness is proportional to the dust column density along the line of sight. If the bow shock is physically thin we can expect that the column density becomes the highest where the bow shock layer intersects with the plane of sky including the central star, based on dust radiative transfer calculations (e.g. Ueta & Meixner 2003). Hence, one can confidently determine the orientation of the bow shock cone by fitting the apparent bow shock shape with the Wilkin bow shock cone equation (eqn.1), taking into account the inclination angle of the bow. This *Wilkin solution fitting*, therefore, would yield the heliocentric orientation of the bow shock cone with respect to the observer. This orientation of the bow represents a relative motion between the mass-losing central star and the ISM local to the star. At the same time, the central star's heliocentric space motion can be defined observationally via measurements of its proper-motion and radial velocity. Naturally, the probability of detecting a bow shock is increased if the star has a large space motion.

Here, we have two vectors of motion concerning a mass-losing star and its ambient ISM. One is the heliocentric relative motion of the star with respect to the ambient ISM and the other is the star's heliocentric space motion. These two vectors are not necessarily the same because the ambient ISM can move/flow into a certain direction irrespective of the star's space motion. Therefore, if one compares the result of the Wilkin solution fitting of the bow shock shape (i.e. the heliocentric relative motion of the mass-losing central star with the ambient ISM) and the observed space motion of the mass-losing central star (i.e. the heliocentric space motion of the star), one can deduce the heliocentric flow vector of the ambient ISM in principle.

3. Wilkin Solution Fitting

Now, we would like to review the potential of this investigation into the heliocentric flow vector of the ambient ISM, which is local to a mass-losing moving star, based on the Wilkin solution fitting (Wilkin 1996) to the apparent bow shock shape for the following cases of three particular stars.

3.1. Betelgeuse (Red Supergiant)

Using the *AKARI*/FIS image at the most sensitive WIDE-S (90μm) band (second from left in Figure 2), the best-fit of the Wilkin solution fitting yields the inclination angle of the bow shock cone with respect to the plane of the sky ($\theta_{\rm incl}$) of $\pm(56^\circ \pm 4^\circ)$, position angle of $55^\circ \pm 2^\circ$ (east of north), and stand-off distance of $4\farcm8 \pm 0\farcm1$. The leading $\pm$ sign of $\theta_{\rm incl}$ indicates the unresolvable degeneracy of the fitting, i.e., the bow shock cone points either away from or to us but the fitting is unable to determine which. Nevertheless, the Wilkin fitting defines a space motion vector of the star *relative to* the ambient ISM (albeit the degeneracy), which we define as $\mathbf{v}_{*\rm ISM}$.

Meanwhile, using the most recent, multi-epoch proper-motion study of Betelgeuse using VLA data, Harper, Brown, & Guinan (2008) derived $(v_\alpha, v_\delta) = (23.3, 8.9)$ km s^{-1} at 197pc. With the average radial velocity of the star ($v_{\rm rad}$) at 20.4 ± 0.4 km s^{-1} (pointed away from us), these numbers yield another space motion vector of the star having $\theta_{\rm incl} = 40^\circ$ and the position angle of 69°. This space motion vector is of course *relative to* the Sun (i.e., the heliocentric correction applied), which we denote as $\mathbf{v}_{*\odot}$. Using these two space motion vectors of the star in two distinct frames, we can then derive the heliocentric flow vector of the ambient ISM, $\mathbf{v}_{\rm ISM\odot}$, by

$$\mathbf{v}_{\rm ISM\odot} = \mathbf{v}_{*\odot} - \mathbf{v}_{*\rm ISM}. \tag{3}$$

Before we proceed any further, however, we have to break the degeneracy of $\mathbf{v}_{*\rm ISM}$. Since Betelgeuse is in the vicinity of the Orion Nebula Complex (ONC), we have relatively complete information about its local environment (e.g. O'Dell (2001)). One of the bases for the present study is the presumed existence of the ISM flow local to the mass-losing moving star. Therefore, there must exist a source of this ISM flow, and the star forming regions in the ONC are most likely. If we assume there is an overall isotropic outflow from the ONC, Betelgeuse's proper motion suggests that it has been traversing across this ISM flow in front

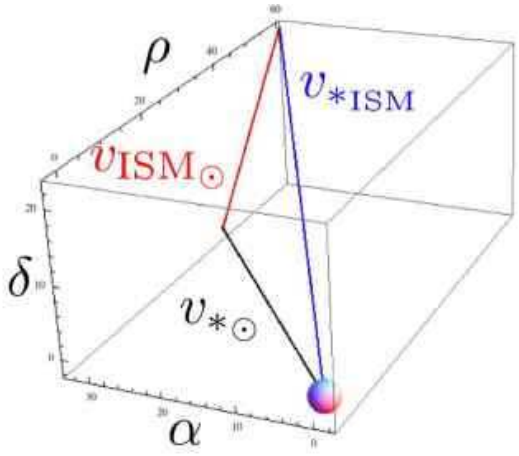

Figure 3. 3-D relationship among the heliocentric space motion of Betelgeuse ($\mathbf{v}_{*\odot}$), heliocentric flow of the ambient ISM ($\mathbf{v}_{\rm ISM\odot}$), and space motion of Betelgeuse relative to the ambient ISM ($\mathbf{v}_{*\rm ISM}$). The sphere at the lower right corner indicates the position of Betelgeuse at the origin of the equatorial coordinates (α, δ, ρ).

of the ONC (see Figure 4 of Harper, Brown, & Guinan 2008). If this is the case, the apex of the bow shock cone around Betelgeuse should point *away from us*, i.e., $\theta_{\rm incl} = -(56^\circ \pm 4^\circ)$. Thus, the degeneracy is lifted and relevant quantities are only dependent on the ambient ISM density, $\rho_{\rm ISM}$.

Using $R_0 = 0.3$pc (Ueta et al. 2008) and $\dot{M} = 3\times10^{-6}$ M$_\odot$ yr^{-1} as derived by Harper, Brown, & Guinan (2008) at the best-estimated distance of 197pc to Betelgeuse and $v_{\rm w} = 17$ km s^{-1} (Bernat et al. 1979), Betelgeuse's space motion with respect to the ambient ISM turns out to be

$$\mathbf{v}_{*\rm ISM} = \begin{pmatrix} v_{\rm rad} \\ v_\alpha \\ v_\delta \end{pmatrix} = \frac{1}{\sqrt{n_{\rm ISM}}} \begin{pmatrix} 32.7 \\ 18.1 \\ 12.7 \end{pmatrix} = \begin{pmatrix} 59.7 \\ 33.0 \\ 23.2 \end{pmatrix} \quad ({\rm km\ s^{-1}}). \tag{4}$$

At the last step, we adopt the ISM number density in front of the ONC, $n_{\rm ISM} = 0.3$ cm^{-3} (Frisch, Sembach, & York 1990). Therefore, the heliocentric ambient ISM flow at Betelgeuse is

$$\mathbf{v}_{\rm ISM\odot} = \mathbf{v}_{*\odot} - \mathbf{v}_{*\rm ISM} = \begin{pmatrix} 20.7 \\ 23.3 \\ 8.9 \end{pmatrix} - \begin{pmatrix} 59.7 \\ 33.0 \\ 23.2 \end{pmatrix} = \begin{pmatrix} -39.1 \\ -9.7 \\ -14.2 \end{pmatrix} \quad ({\rm km\ s^{-1}}) \tag{5}$$

with $v_{*\odot} = 32.4$ km s^{-1}, $v_{*\rm ISM} = 72.1$ km s^{-1}, and $v_{\rm ISM\odot} = 42.7$ km s^{-1}. 3-D relationship among these three vectors is shown in Figure 3. Hence, Betelgeuse is traversing across the ambient ISM flow (of 42.7 km s^{-1}) at the heliocentric space velocity of 32.4 km s^{-1}, resulting in the space velocity relative to the ambient ISM at 72.1km s^{-1}. In the frame of stellar winds, therefore, the flow velocity of the ambient ISM is 89.1 km s^{-1}, which can induce a strong shock.

Betelgeuse is located about 200 pc away from the ONC. At 89.1 km s^{-1} the crossing time is roughly 2.2 Myr, which is consistent with the crossing time of Betelgeuse in front of the ONC. Thus, the assumption of an outflow from the ONC being responsible for the stellar wind-ISM bow shock of Betelgeuse is indeed plausible in retrospect.

3.2. R Hydrae (AGB Star)

Using the *Spitzer* 70μm map (top left in Figure 1), the best-fit of the Wilkin solution fitting yields $\theta_{\rm incl} = \pm(59^\circ \pm 4^\circ)$ and the position angle of $-62^\circ \pm 3^\circ$, defining $\mathbf{v}_{*\rm ISM}$. The stand-off distance of $1\farcm6 \pm 0\farcm1$ translates to 0.1pc at the adopted distance of 165pc (Zijlstra, Bedding, & Mattei 2002). The updated *Hipparcos* proper motion measurements by van Leeuwen (2007) give $(v_\alpha, v_\delta) = (-45.1, 10.1)$ km s^{-1} at 165pc. With $v_{\rm rad} = -10.4$ km s^{-1} (pointed to us), another space motion vector has $\theta_{\rm incl} = 13^\circ$ and the position angle of -77°.

Recent CO observations have revealed a lopsided emission profile, indicating that there is a larger amount of receding matter than approaching matter (Teyssier et al. 2006). In context of a bow shock cone, this means that the cone is pointed away from us (hence more of the receding component). With this the degeneracy of $\mathbf{v}_{*\rm ISM}$ is removed and we derive

$$\mathbf{v}_{\rm ISM\odot} = \begin{pmatrix} v_{\rm rad} \\ v_\alpha \\ v_\delta \end{pmatrix} = \begin{pmatrix} -10.4 \\ -45.1 \\ 10.1 \end{pmatrix} - \frac{1}{\sqrt{n_{\rm ISM}}} \begin{pmatrix} 29.9 \\ -17.5 \\ 3.9 \end{pmatrix} \quad (\text{km s}^{-1}) \qquad (6)$$

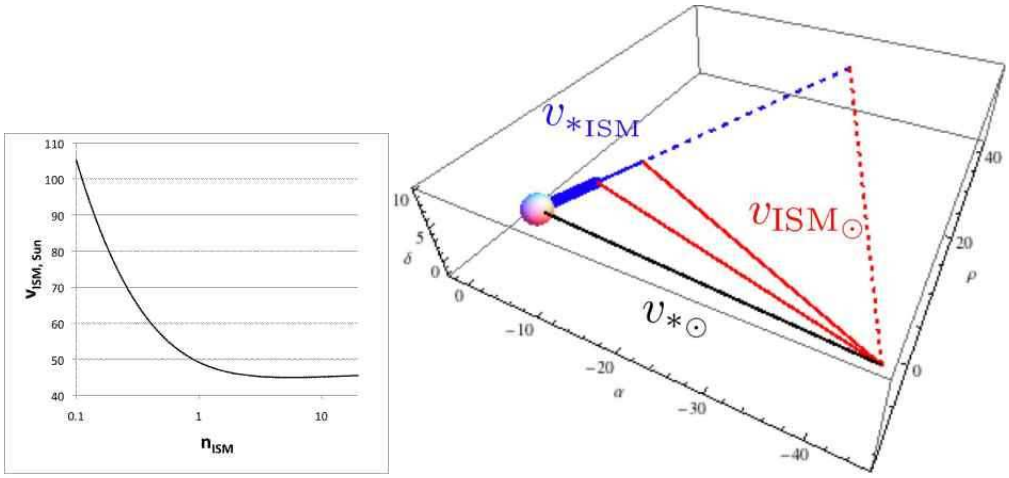

Figure 4. [Left] The $\mathbf{v}_{\rm ISM\odot}$-$n_{\rm ISM}$ plot for R Hya showing behavior of $\mathbf{v}_{\rm ISM\odot}$ as a function of $n_{\rm ISM}$. [Right] 3-D relationship among $\mathbf{v}_{*\odot}$ $\mathbf{v}_{\rm ISM\odot}$ and $\mathbf{v}_{*\rm ISM}$ for R Hya and its ambient ISM. The sphere at the lower left corner indicates the position of R Hya at the origin of the equatorial coordinates (α, δ, ρ). Depending on the choice of the unknown $n_{\rm ISM}$ involved in $\mathbf{v}_{*\rm ISM}$, the solution to $\mathbf{v}_{\rm ISM\odot}$ differs. Displayed are (1) $n_{\rm ISM} = 20$ cm^{-3} (thick solid line, $\mathbf{v}_{*\rm ISM} = 7.8$ km s^{-1}), (2) $n_{\rm ISM} = 5$ cm^{-3} (solid line, $\mathbf{v}_{*\rm ISM} = 14.2$ km s^{-1}), and (3) $n_{\rm ISM} = 0.5$ cm^{-3} (dashed line, $\mathbf{v}_{*\rm ISM} = 49.0$ km s^{-1}).

as a function of the remaining unknown, $n_{\rm ISM}$. Unfortunately there is no definite observational diagnostic for the value of $n_{\rm ISM}$.

However, the $\mathbf{v}_{\rm ISM\odot}$-$n_{\rm ISM}$ plot (Figure 4, left panel) shows that the minimum value of $v_{\rm ISM\odot}$ is 45.0 km s^{-1} when $n_{\rm ISM} = 6$ cm^{-3} and that $v_{\rm ISM\odot}$ remains roughly ~ 45.0 km s^{-1} for larger $n_{\rm ISM}$ but increases for smaller $n_{\rm ISM}$. 3-D relationship among these three vectors is shown for three different values of $n_{\rm ISM}$ (Figure 4, right panel). The space velocity of R Hya relative to the ambient ISM is $34.9/\sqrt{n_{\rm ISM}}$ km s^{-1}, and hence, the smaller $n_{\rm ISM}$ becomes the larger $v_{*\rm ISM}$ becomes. In the frame of stellar winds ($v_{\rm w} = 10$ km s^{-1}, Knapp et al. 1998), therefore, the flow velocity of the ambient ISM with respect to R Hya is $10 + 34.9/\sqrt{n_{\rm ISM}}$ km s^{-1}, which can reach ~ 50 km s^{-1} for $n_{\rm ISM} < 0.8$ cm^{-3}. Typically lower $n_{\rm ISM}$ values are preferred for high galactic latitude objects such as R Hya. Thus, the $v_{\rm ISM\odot}$ value (and hence, the ISM flow velocity relative to R Hya) can be even higher. The next step in this line of research is to establish shock diagnostics for low density, low velocity shocks and obtain the shock velocity in order to fix $n_{\rm ISM}$. This will present a new technique to probe local ISM, complementing previous work such as Lallement et al. (2003).

3.3. R Cassiopeiae (AGB Star)

Far-IR images of R Cassiopeiae (R Cas) show an elliptically elongated shell around the central star that is located off-center of the shell, but the shell does not show any obvious signature of a bow shock (Ueta et al. 2009). However, the wind crossing time for the shell is much longer than the time it took for the star to move to the current off-center position from the center of the shell at the velocity known from proper motion measurements (van Leeuwen 2007). Thus, we speculate that the shell shape is maintained by the interactions between the stellar winds and ambient ISM and that the absence of an apparent bow shock is due to its inclination angle.

The best-fit of the Wilkin solution fitting yields $\theta_{\rm incl} = \pm(68^\circ \pm 2^\circ)$ and the position angle of $74^\circ \pm 2^\circ$, defining $\mathbf{v}_{*\rm ISM}$. The stand-off distance of $1\farcs4 \pm 0\farcs1$ translates to 0.1pc at the adopted VLBI-measured distance of 176pc (Vlemmings, van Langevelde, & Diamo 2005). The updated *Hipparcos* proper motion measurements by van Leeuwen (2007) give $(v_\alpha, v_\delta) = (71.4, 14.6)$ km s^{-1} at 176pc. With $v_{\rm rad} = -22.9$ km s^{-1} (pointed to us), another space motion vector has $\theta_{\rm incl} = 17.5^\circ$ and the position angle of 78.4°. Keeping the degeneracy of $\mathbf{v}_{*\rm ISM}$ we derive

$$\mathbf{v}_{\rm ISM\odot} = \begin{pmatrix} v_{\rm rad} \\ v_\alpha \\ v_\delta \end{pmatrix} = \begin{pmatrix} -22.9 \\ 71.4 \\ 14.6 \end{pmatrix} - \frac{1}{\sqrt{n_{\rm ISM}}} \begin{pmatrix} \pm 20.9 \\ 7.9 \\ 2.3 \end{pmatrix} \quad ({\rm km\ s^{-1}}) \qquad (7)$$

as a function of the remaining unknown, $n_{\rm ISM}$. The $\mathbf{v}_{\rm ISM\odot}$-$n_{\rm ISM}$ plot in Figure 5 shows that $v_{\rm ISM\odot}$ reaches the minimum of 59.5 km s^{-1} at $n_{\rm ISM} = 0.22$ cm^{-3} when the bow shock cone points to us or of 76.2 km s^{-1} at $n_{\rm ISM} = 18$ cm^{-3} when the bow shock cone points away from us. In the frame of stellar winds at 12 km s^{-1} (Knapp et al. 1998), the space velocity of R Cas relative to the ambient ISM is $12 + 22.5/\sqrt{n_{\rm ISM}}$ km s^{-1}, which can reach 60 km s^{-1} if the bow shock cone is pointed to us and $n_{\rm ISM} = 0.22$ cm^{-3}. For low galactic latitude objects such as R Cas, relatively higher $n_{\rm ISM}$ values are expected. Thus, we may expect a value close to the lower limit of 60 km s^{-1}.

4. Summary

When a bow shock structure is observed around a mass-losing star, the central star's proper motion is often consistent with the direction to the apex of the bow. To the first order, this gives an intuitive picture of the mass-losing star moving in the otherwise stationary ambient ISM. Higher spatial resolution far-IR images of such stellar wind bow shocks now allow detailed fitting of the structure given the analytic shape derived by Wilkin (1996). The Wilkin solution fitting, performed for three particular cases, has demonstrated that the heliocentric space velocity vector of a mass-losing star and the orientation of the bow shock cone do not necessarily align with each other, suggesting the existence of a flow of the ambient ISM local to the star.

Since the Wilkin solution fitting is inherently degenerate and other independent observations are needed to break this degeneracy (i.e. determination the orientation of the bow shock cone with respect to the plane of the sky) and to derive the density of the ambient ISM, the analysis is not self-sufficient. Nevertheless, three cases we have shown here unequivocally indicate that flows of the ambient ISM are rather prevalent and high proper-motion stars are often traversing such ambient ISM flows, generating bow shocks as a result. Therefore, stellar wind-ISM bow shocks are potentially excellent probes of the 3-D ISM dynamics local to these shock structures.

Recent far-IR imaging surveys of mass-losing stars such as *AKARI*'s own MLHES Mission Program (PI: I. Yamamura) and its extension for *Spitzer* (*Spitzer*-MLHES, PI: T. Ueta) have identified a number of sources that seem to possess bow shock structures. Using these data sets, one can additionally learn the stellar wind-ISM interactions besides the mass loss histories (from the undisturbed parts of the extended dust shells) that these investigations are originally designed to do. With *AKARI*'s All-Sky Survey data, there will be even more of

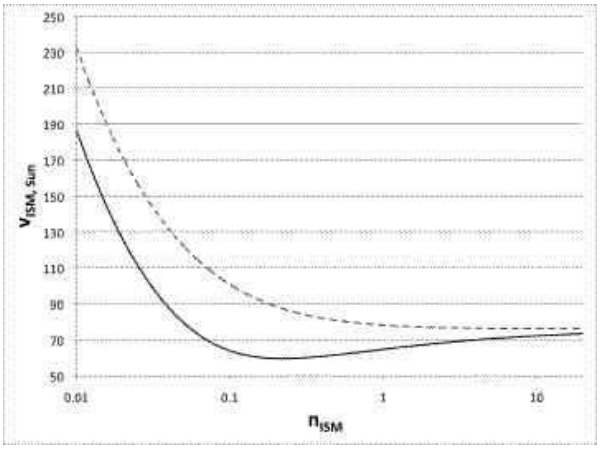

Figure 5. The $\mathbf{v}_{\mathrm{ISM}\odot}$-$n_{\mathrm{ISM}}$ plot for R Cas showing behavior of $\mathbf{v}_{\mathrm{ISM}\odot}$ as a function of n_{ISM}. The solid line is the case where the bow shock cone points to us and the dashed line is the case where the bow shock cone points away from us.

these far-IR bow shocks associated with high proper-motion stars. Therefore, it appears that large-scale investigations of far-IR bow shocks in context of probing the 3-D ISM dynamics should be pursued at least for the solar-neighborhood and we intend to follow up this new avenue of research in near future with existing *AKARI* and *Spitzer* data as well as data from near-future opportunities such as *Herschel Space Observatory* and *Stratospheric Observatory for Infrared Astronomy*.

Acknowledgments. This research is based on observations with *AKARI*, a JAXA project with the participation of ESA, and the *Spitzer Space Telescope*, which is operated by JPL/Caltech under a contract with NASA. Support for this work was provided by University of Denver, ISAS/JAXA, and NASA via JPL/Caltech.

References

Bernat, A. P., et al. 1979, ApJ, 233, L135
Blondin, J. M., & Koerwer, J. F. 1998, New Astron., 3, 571
Dgani, R., Van Buren, D., & Noriega-Crespo, A. 1996, ApJ, 461, 927
Frisch, P. C., Sembach, K., & York, D. G. 1990, ApJ, 364, 540
Gaustad, J. E., et al. 2001, PASP, 113, 1326
Hashimoto, O., & Izumiura, H. 1997, Ap&SS, 255, 349
Harper, G. M., Brown, A., & Guinan, E. F. 2008, AJ, 135, 1430
Kawada, M., et al. 2007, PASJ, 59, S389
Knapp, G. R., et al. 1998, ApJS, 117, 209
Kudritzki, R.-P., & Puls, J. 2000, ARA&A, 38, 613
Lallement, R., et al. 2003, A&A, 411, 447
Mac Low, M.-M., et al. 1991, ApJ, 369, 395
Matsuura, M., et al. 2009, MNRAS, in press
Murakami, H., et al. 2007, PASJ, 59, S369
O'Dell, C. R. 2001, ARA&A, 39, 99
Sedlmayr, E. 1994, in Lecture Notes in Physics, 428, 163
Stencel, R. E., Pesce, J. E., & Hagen Bauer, W. 1988, AJ, 95, 141
Teyssier, D., et al. 2006, A&A, 450, 167
Ueta, T., & Meixner, M. 2003, ApJ, 586, 1338
Ueta, T., et al. 2006, ApJ, 648, L39
Ueta, T., et al. 2008, PASJ, 60, S407
Ueta, T., et al. 2009, in this volume
Van Buren, D., & McCray, R. 1988, ApJ, 329, L93
van Leeuwen, F. 2007, A&A, 474, 653
Vlemmings, W. H. T., van Langevelde, H. J., & Diamond, P. J. 2005, A&A, 434, 1029
Wareing, C. J., Zijlstra, A. A. & O'Brien, T. J. 2007, ApJ, 660, L129
Werner et al. 2004, ApJS, 154, 1
Wilkin, F. P. 1996, ApJ, 459, L31
Wilkin, F. P. 2000, ApJ, 532, 400
Willson, L. A. 2000, ARA&A, 38, 573
Zijlstra, A. A., Bedding, T. R., & Mattei, J. A. 2002, MNRAS, 334, 498